Conjugation Length Effect on the Conducting Behaviour of Single-crystalline Oligo(3,4-ethylenedioxythiophene) (*n*EDOT) Radical Cation Salts

Ryohei Kameyama, Tomoko Fujino,* Shun Dekura, and Hatsumi Mori*

Table of Contents

1. General

All manipulations of oxygen- and moisture-sensitive materials were conducted with a standard schlenk technique under an argon atmosphere. Analytical thin layer chromatography (TLC) was performed on a glass plate coated with silica gel (230–400 mesh, 0.25 mm thickness) containing a fluorescent indicator (silica gel $60F_{254}$, Merck). Flash silica gel column chromatography[1] was performed on commercial packed column, Biotage® SNAP Ultra.

2. Apparatus

Proton and carbon nuclear magnetic resonance (^{1}H and ^{13}C NMR) spectra were recorded on a JEOL JNM-AL300 (^{1}H NMR: 300 MHz; ^{13}C NMR: 75 MHz) spectrometer with solvent resonance as the internal standard (^{1}H NMR, $Si(CH_3)_4$ at 0.00 ppm; ^{13}C NMR, $Si(CH_3)_4$ at 0.0 ppm). ^{1}H NMR data are reported as follows: chemical shift, multiplicity, *J*-coupling constants (Hz), and relative integrated intensity. High-resolution mass spectra (HRMS) were obtained using a JEOL JMS-AX500 with a field desorption (FD) probe at the positive mode using cholesterol as an internal standard. Single-crystal X-ray diffraction (XRD) measurements were performed using a Rigaku MercuryII CCD X-ray diffractometer (XRD, Mo K_α, λ = 0.71073 Å). Elemental analysis (CHN compositions) was performed using an Elementar Vario MICRO CUBE analyzer. Cyclic voltammetry analyses were performed using an ALS 610DB electrochemical analyzer. Resistivity measurements were performed on HUSO HECS 994C with a high-resistance-low-current electrometer (KEYTHLEY 6517B) and a digital multimeter (KEYTHELY 2001). The X-band continuous wave ESR experiments were performed using a Bruker EMXmicro spectrometer. The static magnetic susceptibility measurements were performed using a Quantum Design SQUID magnetometer (MPMS-XL).

3. Materials

The following reagents were purchased from commercial suppliers and used as received: palladium acetate (Tokyo Chemical Industry), pivalic acid (Wako Pure Chemical Industries), anhydrous potassium carbonate (Wako Pure Chemical Industries), super dehydrated *N*,*N*-dimethylformamide (DMF, Wako Pure Chemical Industries), tetra-*n*-

butylammonium hexafluorophosphate (n-Bu_4NPF_6, Aldrich), carbon paste (XC-12, DOTITE, Fujikura Kasei), silver paste (D-500, DOTITE, Fujikura Kasei), and ethylene glycol monobutyl ether acetate (Tokyo Chemical Industry). Compounds **1**,[2] **2a**[3] and **2b**[4] were synthesized according to the reported procedures.

4. Synthesis

Synthesis of donor **3O** (2MeS-3EDOT)

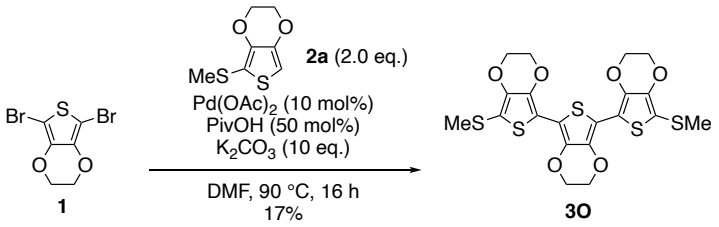

Referring to the reported procedure for the Pd-catalyzed C-H arylation,[5] **3O** was synthesized. Thus, to the mixture of palladium(II) acetate (11.8 mg, 52.6 μmol), potassium carbonate (727 mg, 5.26 mmol) in dry DMF (4 mL) was added a solution of 2,5-dibromo(3,4-ethylenedioxythiophene) **1** (158 mg, 526 μmol), 2-methylthio(3,4-ethylenedioxythiophene) **2a** (198 mg, 1.05 mmol), and pivalic acid (26.8 mg, 262 μmol) in dry DMF (4 mL), and the mixture was heated at 90 °C for 16 h. The mixture was allowed to cool to ambient temperature and extracted with dichloromethane (50 mL). The solution was washed with water (2 × 20 mL) and brine (20 mL) and dried over Na_2SO_4. After removal of volatile materials in vacuo, the crude material was purified by flash column chromatography (eluent: 80–100% v/v dichloromethane/hexane) to give the title compound as a yellow solid (45.3 mg, 88.0 μmol, 17%). Physical data of **3O**: ^{1}H NMR ($CDCl_3$, 300 MHz) δ 2.39 (s, 6H), 4.39–4.32 (m, 12H); ^{13}C NMR ($CDCl_3$, 75 MHz) δ 21.5, 64.8, 65.01, 65.04, 112.4, 136.2, 137.0, 142.9. Two sp^2 carbons were not detected due to the overlaps to solvent peaks or low solubility of the compound. The integrity of the compound was confirmed by HRMS analysis: HRMS (FD+) calcd for $C_{20}H_{18}O_6S_5$ [$M^{\bullet+}$] 513.9701, found 513.9721, and XRD analysis of the single crystal obtained from recrystallization of **3O** by liquid-liquid diffusion method using chloroform and ethanol (Tables S1, S2, and Figure S2). The high purity of the compound was confirmed by NMR spectra (Figures S13 and S14).

Synthesis of donor **3O-SHex** (2HexS-3EDOT)

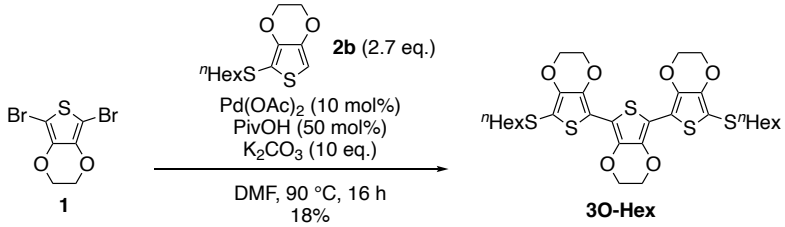

The soluble analog **3O-SHex** was synthesized likewise in **3O** synthesis except using **2b** instead of **2a**. To the mixture of palladium(II) acetate (4.4 mg, 20 μmol), potassium carbonate (302 mg, 2.19 mmol) in dry DMF (4 mL) was added a solution of 2,5-dibromo(3,4-ethylenedioxythiophene) **1** (65.6 mg, 219 μmol), 2-hexylthio(3,4-ethylenedioxythiophene) **2b** (151 mg, 586 μmol), and pivalic acid (11.2 mg, 110 μmol) in dry DMF (4 mL) at ambient temperature, and the mixture was heated at 90 °C for 16 h. The mixture was allowed to cool to ambient temperature and extracted with dichloromethane (50 mL). The solution was washed with water (2 × 20 mL) and brine (20 mL) and dried over Na_2SO_4. After removal of volatile materials in vacuo, the crude material was purified by flash column chromatography (eluent: 80–100% v/v dichloromethane/hexane) to give the title compound as a yellow solid (26.1 mg, 39.9 μmol, 18%). Physical data of **3O-SHex**: ^{1}H NMR ($CDCl_3$, 300 MHz) δ 0.88 (t, J = 6.2 Hz, 6H), 1.20–1.50 (m, 12H), 1.50–1.72 (m, 4H), 2.73 (t, J = 7.3 Hz, 4H), 4.25–4.40 (m, 12H); ^{13}C NMR ($CDCl_3$, 75 MHz) δ 14.1, 22.5, 28.2, 29.5, 31.4, 38.2, 64.8, 64.96, 65.01, 104.9, 108.3, 112.7, 136.1, 137.0, 143.4. The structural integrity and purity were identified by NMR spectra (Figures S15 and S16) and HRMS (FD+) calcd for $C_{30}H_{38}O_6S_5$ [$M^{\bullet+}$] 654.1266, found 654.1297.

Synthesis of radical cation salts **3O**•$PF_6(CH_2Cl_2)_n$ (**3O**•hexafluorophosphate)

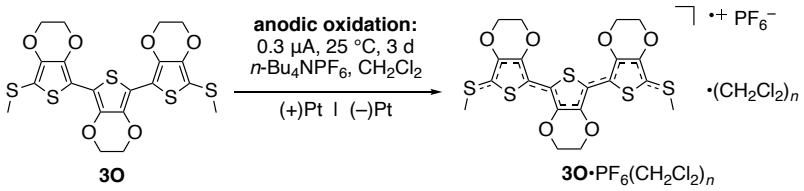

A donor **3O** (5.1 mg, 10 μmol) was placed in one side of an H-shaped cell equipped with a glass filter and *n*-Bu_4NPF_6 (2 × 10 mg) were placed in each side of the cell, respectively. The compounds were dissolved in degassed dichloromethane (10 mL) under ultrasonic irradiation for >10 min. Two pre-annealed platinum electrodes were inserted into each side of the cell, and the cell was kept at 25 °C for 2 hours. Then, a constant current of 0.3 μA was applied to the solution at 25 °C for 3 days to afford black needle-like crystals of **3O**•$PF_6(CH_2Cl_2)_n$ (typical size: 0.20 × 0.03 × 0.03 mm^3). The crystal structures and chemical compositions, from which the solvent molecules were excluded, were identified by single-crystal X-ray structural analyses (Tables S1, S2, and Figure S3). The composition was determined by the elemental analysis (CHN composition) using calibration curves based on the integrated intensity obtained: calcd for **3O**•$PF_6(CH_2Cl_2)_{0.5}$ ($C_{20.5}H_{19}ClF_6O_6PS_5$), C 35.07%; H 2.73%; N 0.00%, found: C 35.38%; H 3.02%; N 0.30%. This data suggests the presence of 0.5 equivalent of dichloromethane solvents per donor.

5. Cyclic voltammetry analyses

We used a degassed 500 mM solution of **2O-SHex**[6] and **3O-SHex** in 1:1 v/v dichloromethane/acetonitrile containing 50 mM *n*-Bu_4NPF_6. We used a glassy carbon as the working electrode, a platinum wire as the counter electrode, and a silver-silver chloride electrode (Ag/AgCl/1 M KCl) as the reference electrode. The scan rate was set as 0.1 V s^{-1}. The reduction potentials for **3O–SHex** could not be identified because the reductive peaks were overlapped because of the poor solubility of the oxidized species.

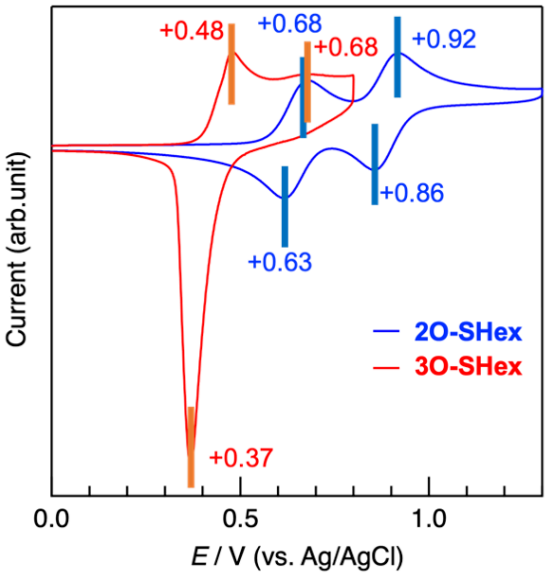

Figure S1. Cyclic voltammograms of **2O-SHex** and **3O-SHex**.

6. Single-crystal X-ray diffraction (XRD) structural analyses

The single-crystal structure of **3O**•$PF_6(CH_2Cl_2)_n$ was analyzed by a direct method (SHELXT[7] version 2018/2) and refined with full-matrix least-squares technique (SHELXL version 2018/3) using an Olex2[8]-1.2 (OlexSys) software. Anisotropic thermal parameters were applied to all non-hydrogen atoms. The hydrogen atoms were generated geometrically. Ethylene groups of outer EDOT units in **3O** were disordered with the occupancy of 68:32. The groups for the outer/inner units and PF_6 anions of **3O**•$PF_6(CH_2Cl_2)$ were disordered in the occupancies of 53:47/50:50 and 50:50, respectively. The disordered solvent molecules are excluded in the structural analysis by the solvent mask option implemented in Olex2, and therefore the resulting formula, formula weight, and density did not include the information of the crystal solvent. The **3O** crystals used in the XRD crystal structure analysis were twinned, so we analyzed the data as a sum of two single crystals (BASF parameter: 0.499(4)).

Table S1. Crystallographic data for single crystals of **3O** and **3O**•$PF_6(CH_2Cl_2)_n$. [a]The data excludes the solvent molecules by the structural analysis with solvent mask option.

Compounds	**3O**	**3O**•$PF_6(CH_2Cl_2)_n$
Temperature / K	293	293
Formula	$C_{20}H_{18}O_6S_5$	$C_{20}H_{18}O_6F_6PS_5$[a]
Formula weight	514.64	659.61[a]
Crystal system	*monoclinic*	*monoclinic*
Space group	*I*2/*a* (#15-3)	*C*2/*m* (#12)
a / Å	8.1299(9)	13.4985(13)
b / Å	16.3935(15)	29.366(2)
c / Å	16.5034(13)	7.0331(6)
α / deg.	90	90
β / deg.	95.897(9)	102.400(9)
γ / deg.	90	90
V / Å^3	2187.9(4)	2722.9(4)
Z	4	4
D_{calc} / g cm^{-3}	1.562	1.609[a]
R_{int}	0.0600	0.0494
R_1 ($I > 2.00\sigma(I)$)	0.0887	0.0568
wR_2 (all reflections)	0.2723	0.1602
GOF	1.124	1.041
CCDC	2123081	2123091

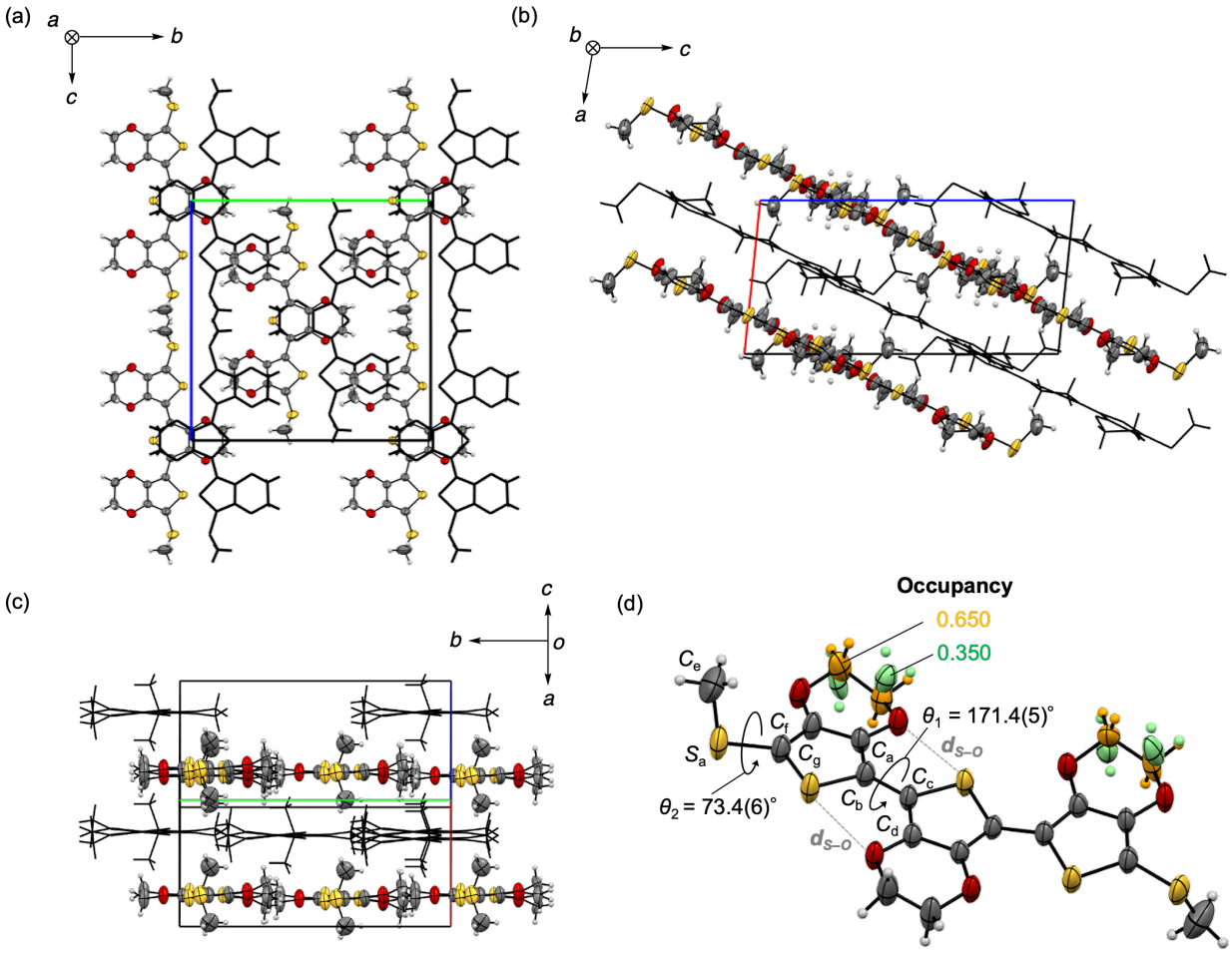

Figure S2. ORTEP drawings (50% thermal ellipsoid) and black wire models in the packing structure of **3O** (a half crystallographically independent molecule was contained in the unit cell). (a, b) The molecular arrangements were shown along the *a*-axis (a), the *b*-axis (b), and the π-plane (c). (d) Enlarged molecular structure of **3O**. θ_1 is a twist angle between the thiophene rings (i.e., C_a-C_b-C_c-C_d). θ_2 is a torsion angle between the MeS–C bond (i.e., C_e-S_a-C_f-C_g). Yellow: sulfur, red: oxygen, grey: carbon, white: hydrogen.

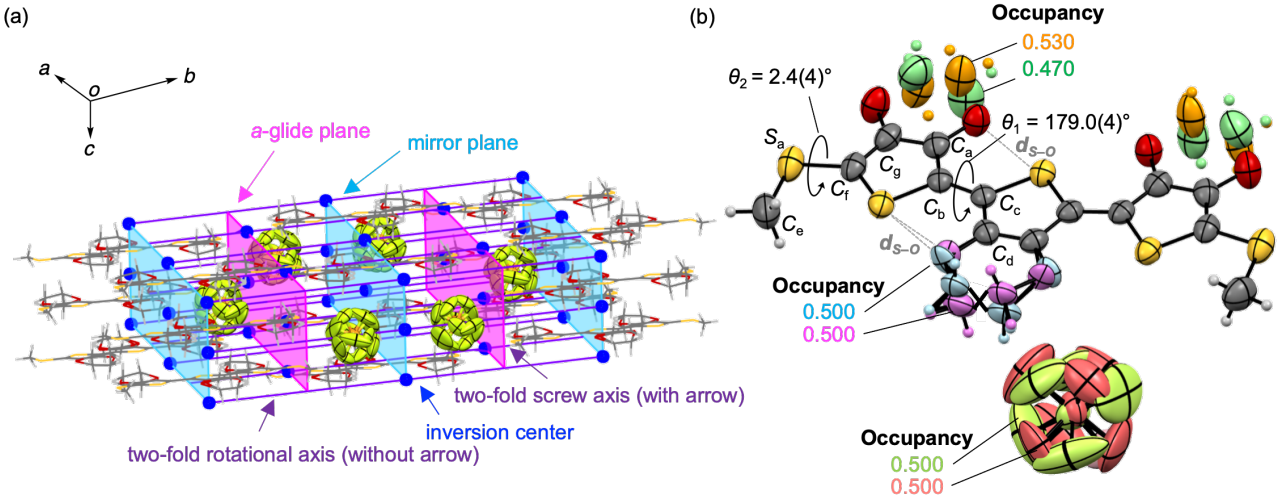

Figure S3. Structure of **3O**•$PF_6(CH_2Cl_2)_n$ along the *c*-axis. (a) Symmetry elements were displayed with a wireframe style for the donor molecules and ORTEP drawing for the counter anions. Yellow: sulfur, red: oxygen, grey: carbon, white: hydrogen, green: fluorine, orange: phosphorous. (b) Enlarged ORTEP (50% thermal ellipsoid) drawing of the **3O**•$PF_6(CH_2Cl_2)_n$.

Table S2. Structural parameters for the crystal structures of **3O** and **3O**•$PF_6(CH_2Cl_2)_n$.

Compounds	**3O**	**3O**•$PF_6(CH_2Cl_2)_n$
θ_1 / deg.	171.5(5)	179.0(5)
θ_2 / deg.	73.0(6)	2.4(4)
Interplanar distance[b] / Å	3.830	3.441, 3.545
Centroid distance[c] / Å	5.902	3.616, 3.829
$d_{S–O}$[c] / Å	2.901(3), 2.930(3)	2.97(3), 2.73(3), 2.916(3)

[a] θ_1 is a twist angle between the thiophene rings, which was defined as C_a-C_b-C_c-C_d. θ_2 is a torsion angle between the MeS–C bond, which was defined as C_e-S_a-C_f-C_g. [b] The centroid distance was measured between the center of the adjacently facing molecule, i.e., the geometrical center of non-hydrogen atoms (total 31 atoms) of **3O**. [b] The interplanar distance was measured between the mean planes of 15 atoms in three thiophene rings of the facing molecule. [c] The distance of a sulfur atom (thiophene ring) and an oxygen atom (ethylenedioxy group) in **3O** (Figures S2d and S3b).

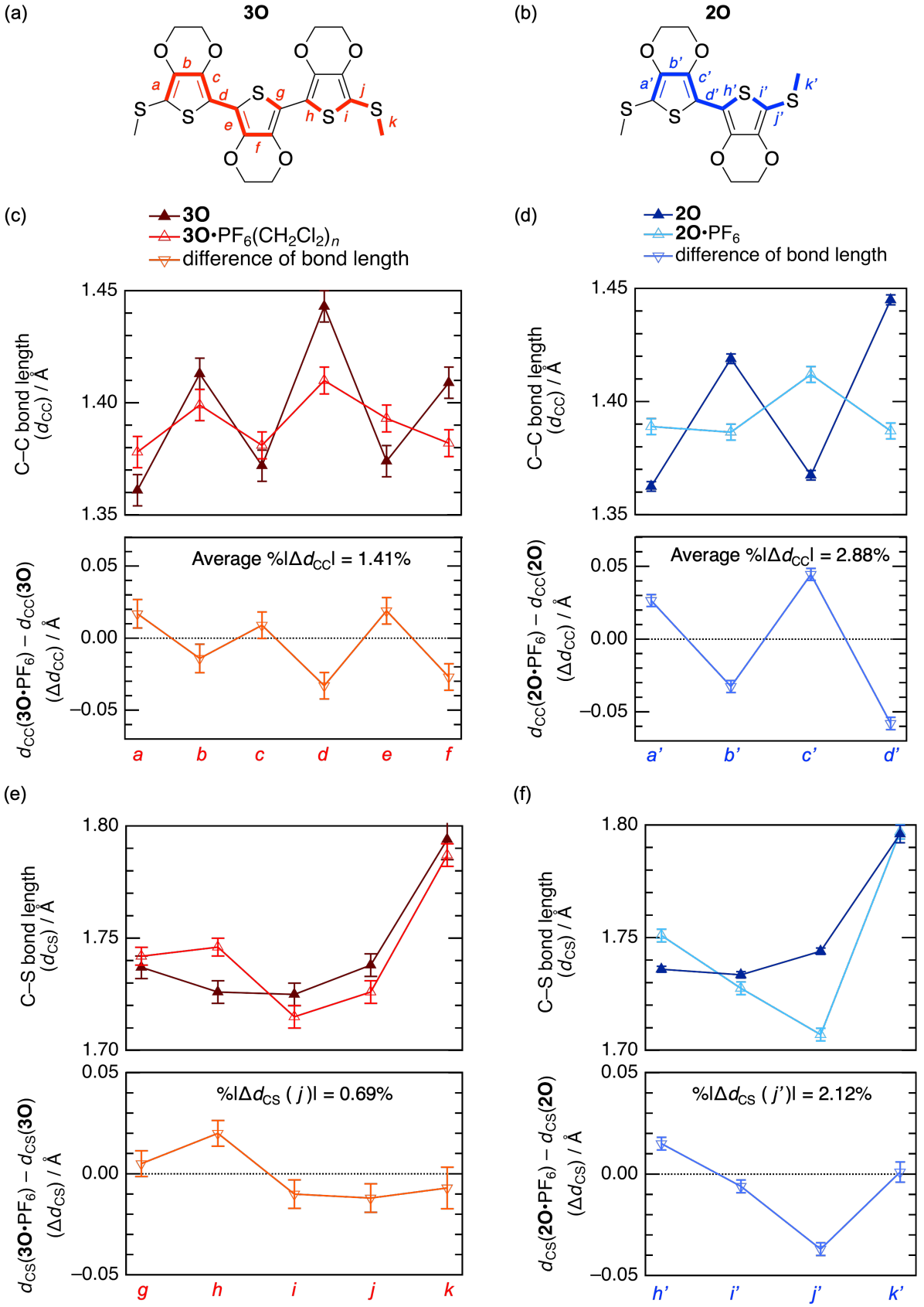

Figure S4. Bond length analysis for single crystals of **3O** (a, c, e) and **2O** (b, d, f) in neutral states and radical cation salt states. (a, b) Labeling of chemical bonds. (c–f) The C–C and C–S bond lengths (d_{CC}, d_{CS}) and of **3O** (c, e) and **2O** (d, f) in forms of neutral states and radical cation salt states, and the difference of d_{CC} and d_{CC} (Δd_{CC} or Δd_{CS}) after oxidation. $\%|\Delta d_{CC}|$ and $\%|\Delta d_{CS}|$ represent the relative absolute values of Δd_{CC} and Δd_{CS} for those of neutral congeners, respectively.

7. Theoretical calculations

7-1. Analysis of SOMO's shape of radical cations

All the calculations were performed on the Gaussian 09 program[9] at the density functional theory (DFT) level with the unrestricted B3LYP functional, the gradient correction of the exchange functional by Becke[10] and the correlation functional by Lee, Yang and Parr.[11] The 6-31G(d) split valence plus polarization basis set was used.[12] Cartesian coordinates for the optimized geometries are shown in Tables S3 and S4. The calculated SOMO shapes of radical cations **3O**$^{\bullet+}$ and **2O**$^{\bullet+}$ were visualized on GaussView 5.0 as shown in Figure S5.

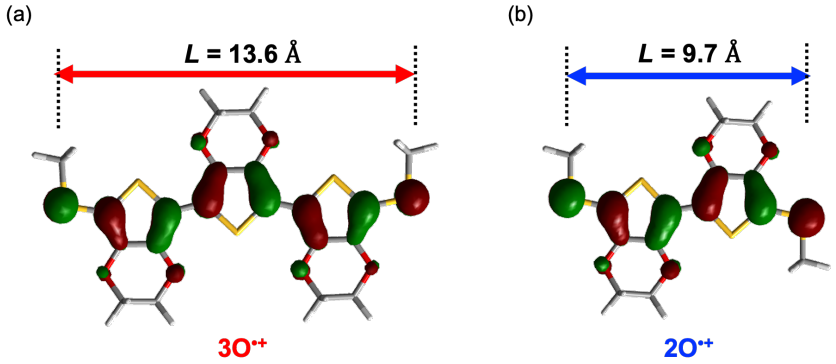

Figure S5. SOMO and molecular size of **3O**$^{\bullet+}$ (a) and **2O**$^{\bullet+}$ (b).

7-2. Overlap and transfer integrals calculations

Intermolecular orbital interactions in the single crystal structure of **3O**•$PF_6(CH_2Cl_2)_n$ were calculated with the extended Hückel method.[13] In the calculation, we used a closed-shell HOMO of **3O** instead of SOMO of **3O**$^{\bullet+}$ and evaluated the overlap integral $|S|$. Thus, we first calculated the HOMO of **3O** based on the geometry of **3O**$^{\bullet+}$ in the **3O**•$PF_6(CH_2Cl_2)_n$ crystal structures at 293 K (Figures S5) without structural optimization. Based on the HOMO, we then estimated the overlap integrals $|S|$ for the interaction between a donor and either of the nearest neighboring six donors (Figure S6). The resulting $|S|$ values were converted to the transfer integrals t using the empirical equation: t = 10 (eV) × $|S|$ (Table 1).

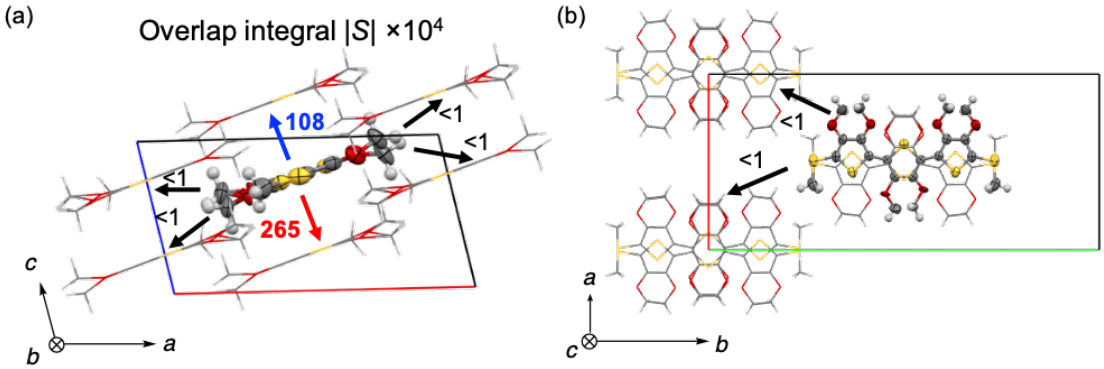

Figure S6. Overlap integrals $|S|$ in the single crystal structure of **3O**•$PF_6(CH_2Cl_2)_n$. Views with calculated $|S|$ were shown along the *b*-axis (a) and the *c*-axis (b), respectively.

7-3. Band structure calculations

All the periodic DFT calculations were performed by the OpenMX software based on optimized localized basis

functions and pseudopotentials. The basis functions used are H6.0-s2p1, C6.0-s2p2d1, O6.0-s2p2d1, and S7.0-s2p2d1f1 for hydrogen, carbon, oxygen, and sulfur respectively, wherein the abbreviation of basis functions such as C6.0-s2p2d1, C stands for the atomic symbol, 6.0 the cutoff radius (Bohr) in the generation by the confinement scheme, and s2p2d1 means the employment of two, two, and one optimized radial functions for the s-, p-, and d-orbitals, respectively. The radial functions were optimized by a variational optimization method.[14,15] As valence electrons in the pseudopotentials (PPs), we included 1s for hydrogen, 2s and 2p for carbon and oxygen, 3s and 3p for phosphorous and sulfur, respectively. All the PPs and pseudo-atomic orbitals (PAOs) we used in the study were taken from the database (2019) in the OpenMX website,[16] which was benchmarked by the delta gauge method.[17] Real space grid techniques are used for the numerical integrations and the solution of the Poisson equation using FFT with the energy cutoff of 220 Ryd.[18] We performed Brillouin-zone integrations on a 3×3×3 k-grid; the Fermi-Dirac distribution function at 300 K is employed as a smeared occupation function. We used a generalized gradient approximation (GGA) proposed by Perdew, Burke, and Ernzerhof to the exchange-correlation functional.[19] In the calculations, the geometries in the single crystal structure of **3O**•$PF_6(CH_2Cl_2)_n$ at 293 K, where the anion structures were excluded, were used without preceding structural optimization. The system charge was set to +4.0 (+1 for each donor molecule) for those that excluded anion structures to compensate the charge balance. The salts **3O**•$PF_6(CH_2Cl_2)_n$ consistently exhibited 1D electronic structure with a half-filled HOCO band (Figures S6).

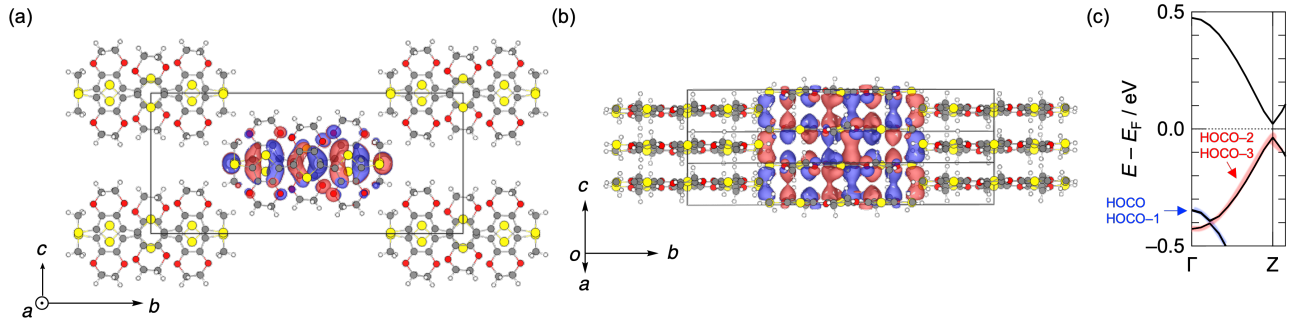

Figure S7. The real parts of HOCO–2 (corresponded to the HOMO of neutral **3O**) of **3O**•$PF_6(CH_2Cl_2)_n$ at the Γ point (0,0,0) in the central column were visualized by VESTA[20] along (a) the *a*-axis and (b) π-plane (b). The total charges of these systems were set as +4.0 (+1 per one donor), respectively. Disordered anions and solvent molecules were excluded from the calculation. Γ (0,0,0), Z (0,0,0.5), X (0.5,0,0), A (0.5,0.5,0), Y (0,0.5, 0). (c) Enlarged view of the band structure of **3O**•$PF_6(CH_2Cl_2)_n$ with the labeling of HOCO and HOCO–*n* bands for clarity. The two bands degenerated due to the presence of two crystallographically equivalent molecules in a unit cell.

8. Electrical resistivity measurements

Electrical resistivity (ρ) measurements of the single crystals of **3O**•$PF_6(CH_2Cl_2)_n$ were performed by the conventional two-probe method. The sample was prepared by attaching gold wires (15 μm diameter) to both ends of the long axis (i.e., the stacking *c*-axis) of a single crystal with a conductive carbon paste. Before temperature (T) -dependent resistance (R) measurement, ohmic behaviors of the samples were confirmed by the current–voltage (I–V) characteristics at room temperature from −10 to 10 V (Figure S8). Within the ohmic region, the temperature-dependent R of the sample was measured at a constant dc voltage (5 V) upon cooling the electrode from room temperature to ca. 10 K and subsequent heating to room temperature (ca. 1 K/min). During the measurements, the temperature of the sample was monitored by the Cernox (Lake Shore) thermometer. The ρ and conductivity (σ) values were derived from the following equation: $\rho\ (= \sigma^{-1}) = RS/L$ (Figure 3a): $S = 900\ \mu m^2$, $L = 232\ \mu m$.

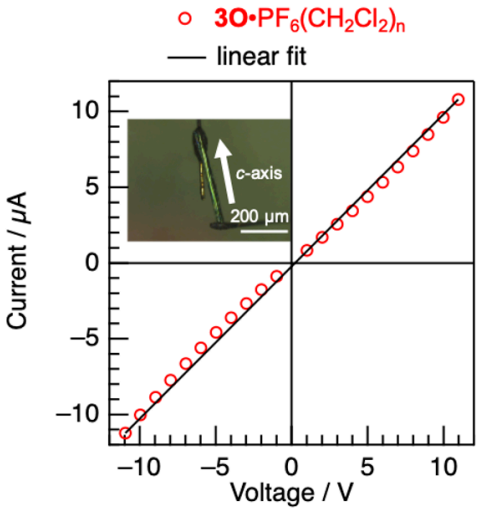

Figure S8. *I–V* curve of **3O**•$PF_6(CH_2Cl_2)_n$ at 293 K between from −10 to 10 V.

9. Electron spin resonance (ESR) measurements

The X-band (~9.4 GHz) continuous wave ESR experiments were performed on single crystals of **2O**·PF_6 and **3O**•$PF_6(CH_2Cl_2)_n$ with field modulation (0.2 G). The ESR signals were measured by rotating the long axis of the crystal (i.e., the stacking *c*-axis) from the direction parallel to the magnetic field (i.e., $\varphi \sim 0°$ or 180°) to the direction perpendicular to the field (i.e., $\varphi \sim 90°$) at 293 K (Figures S9b). The *T*-dependent signals were measured at φ = 90° (perpendicular to the stacking *c*-axis) the signals from 293 K to 4 K (Figures S9a, S10). The spin susceptibility values χ_{spin} were calculated by the following equation (Figure S10):

$$\boldsymbol{\chi_{spin} \propto I_m \times (\Delta B_{pp})^2}$$

, where maximum intensity I_m, the peak-to-peak width ΔB_{pp}, and resonance center B_0 were determined by fitting to the equation of Lorentzian in the differential form as follows.

$$I(B) = \frac{16 I_m (B_0 - B)/(\Delta B_{pp}/2)}{[3 + \{\frac{B_0 - B}{\Delta B_{pp}}/2\}^2]^2}$$

The χ_{spin}–*T* plots of **3O**•$PF_6(CH_2Cl_2)_n$ showed an exponential-like demagnetization curve upon cooling without any significant magnetic transitions (Figure S10a). The curve was fitted using a singlet–triplet (S–T) model and the gap ($2|J|/k_B$) was estimated to be 1103(20) K. In contrast, the χ_{spin}–*T* plots of **2O**•PF_6 showed a demagnetization curve with a paramagnetic-nonmagnetic transition around 220 K (Figure S10b), where the $2|J|/k_B$ value was estimated as 1065(8) K using a singlet-triplet model function:

$$\chi_{spin} \approx \frac{N g^2 \mu_B^2}{k_B T} \frac{1}{3 + exp \frac{2|J|}{k_B T}}$$

The comparable $2|J|/k_B$ value of **3O**•$PF_6(CH_2Cl_2)_n$ to that of **2O**•PF_6 supported the strong intermolecular orbital interaction over electronic correlations[21] with relatively large $\boldsymbol{U_{eff}}$ values (estimated as 1.3–1.5 eV in Figure S11) unique to these radical cation salts of EDOT systems. The relatively narrow ΔB_{pp} (~ 1 G) observed for **3O**•$PF_6(CH_2Cl_2)_n$ and **2O**•PF_6 may also originate in the 1D nature of the spin–spin interaction. It should be noted that the transition observed for **2O**•PF_6 may result from the instability of the 1D uniform spin system that can induce its π-dimerization; **2O**•BF_4 also showed a similar magnetic transition at 170 K, along with the appearance of an undetermined new phase in the low-*T* XRD measurement. The absence of the significant magnetic transition

in **3O**•$PF_6(CH_2Cl_2)_n$ is consistent with the π-dimerized structure at 293 K confirmed by the XRD single crystal structural analysis.

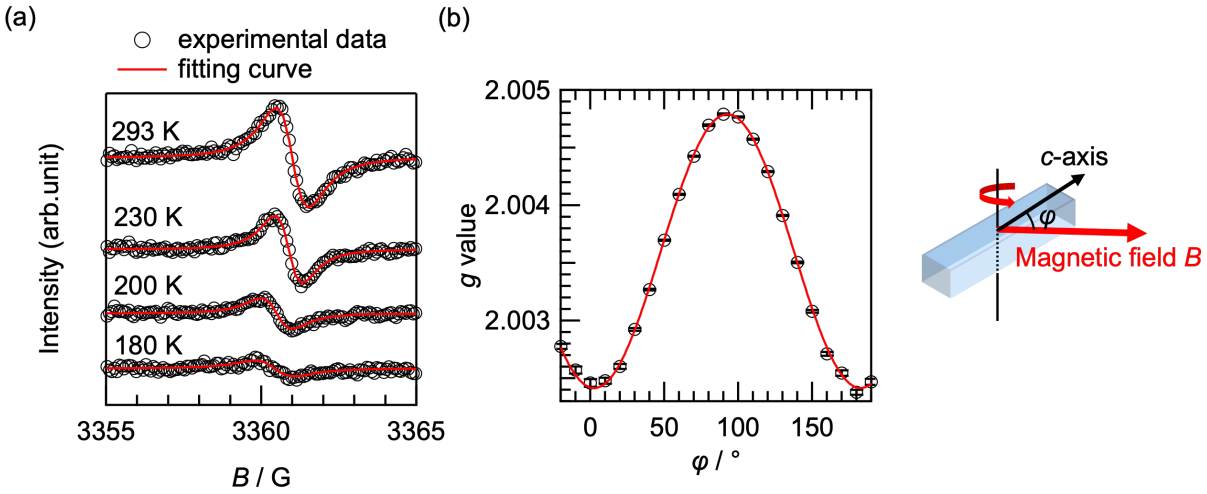

Figure S9. (a) *T*-dependent ESR spectra of **3O**•$PF_6(CH_2Cl_2)_n$ at $\varphi = 90°$ ($g = 2.0048$ at 293 K). (b) ϕ-dependent *g*-values of the **3O**•$PF_6(CH_2Cl_2)_n$ at 293 K.

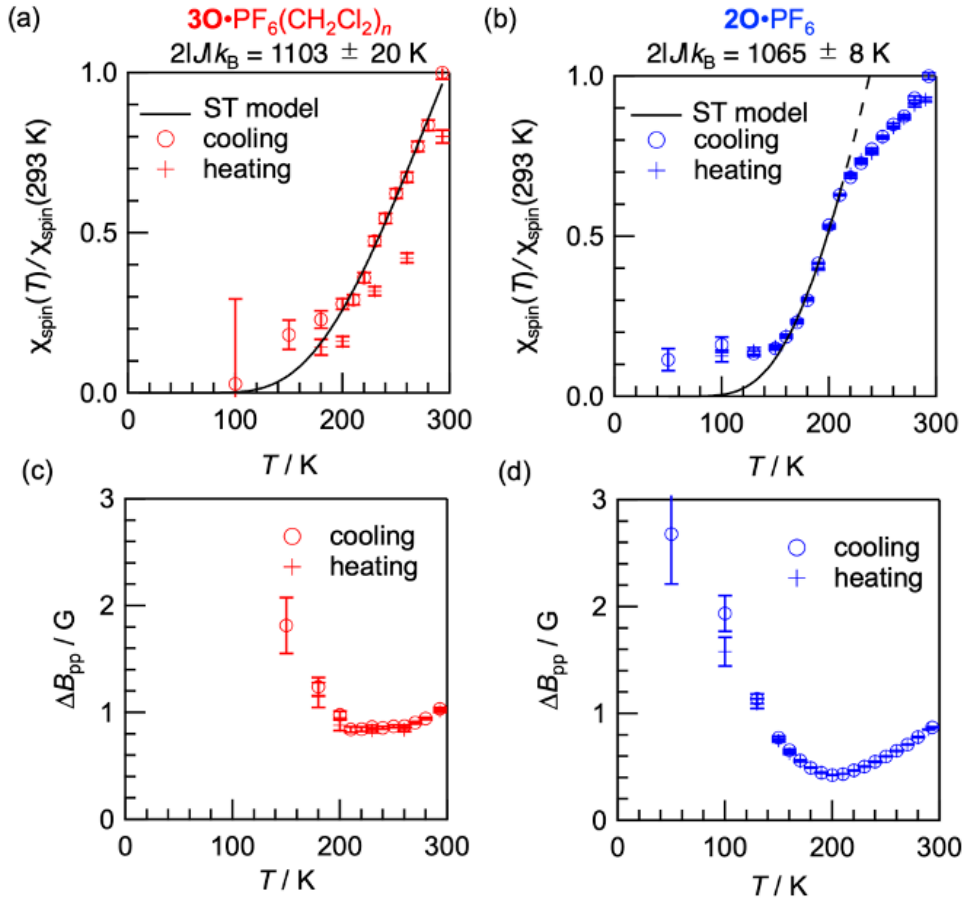

Figure S10. *T*-dependent relative spin susceptibility at $\varphi = 90°$ of **3O**•$PF_6(CH_2Cl_2)_n$ (a) and **2O**•PF_6 (b). Black lines show fitting curves using a S–T model function with $2|J|/k_B$: 1103 ± 20 K (a) and 1065 ± 8 K (b), respectively.

10. Static magnetic susceptibility measurements

The static magnetic susceptibility of poly-crystalline samples of **3O**•$PF_6(CH_2Cl_2)_n$ was measured upon cooling from 300 K to 2 K by <1 K/min applying the static magnetic field of 50,000 Oe. The absence of ferromagnetic impurity in the synthesized samples was confirmed from the obtained *M*–*H* curve at 2 K around −55,000 to 55,000 Oe (Figure S11c). The *M*–*H* curve at 2 K follows a typical Brillouin function. At 2 K, the magnetization saturates at 50,000 Oe, but linearity is expected to be restored in the temperature range above 10 K. The obtained magnetic susceptibilities (χ_{exp}) were plotted after subtracting the contribution of the Curie impurity for $S = 1/2$ (χ_{cw}; 1.1 % for the molar amount of **3O**•$PF_6(CH_2Cl_2)_n$; n was set as 0.5 based on the elemental analysis) and the contribution from core diamagnetism ($\chi_{core} = -3.70 \times 10^{-4}$ emu mol^{-1}) estimated from Pascal's law[22] (Figure S11). The anomaly around 50 K is attributed to the presence of molecular oxygen in the sample holder.

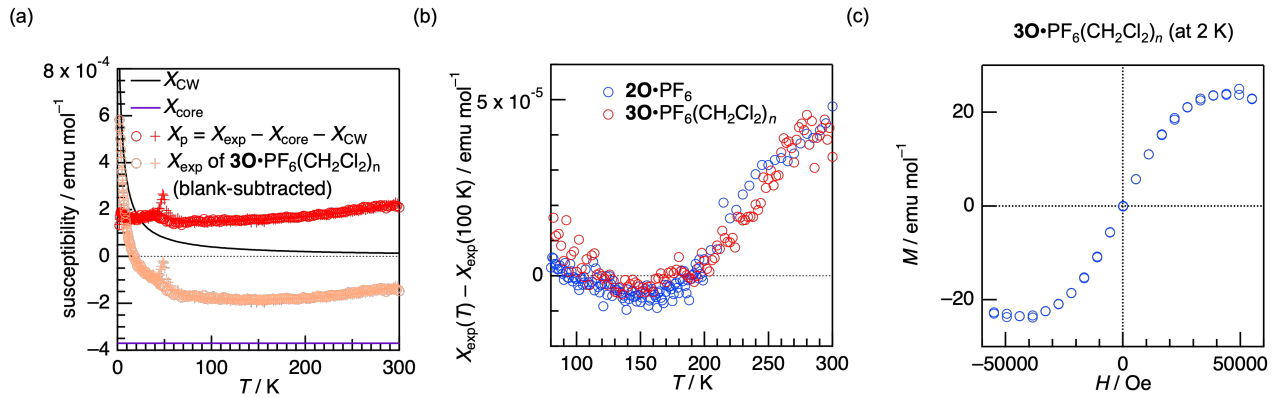

Figure S11. (a) χ_{exp}–T plots of **3O**•$PF_6(CH_2Cl_2)_n$ poly crystals at the static magnetic field of 50,000 Oe. (b) The enlarged and overlapped χ_{exp}–T plots of **3O**•$PF_6(CH_2Cl_2)_n$ and **2O**•PF_6 at cooling process shown in Figures 11a and previous report[23], in which the χ_{exp} values were adjusted by subtracting the value at 100 K based upon the ESR measurement (χ_{spin} ~0 at 100 K, Figure S10a and S10b). (c) *M*–*H* curve of **3O**•$PF_6(CH_2Cl_2)_n$ at 2 K around −55,000 to 55,000 Oe.

11. Estimation of U_{eff}

We estimated and compared U_{eff} values of **3O**•$PF_6(CH_2Cl_2)_n$ and **2O**•PF_6. The values were calculated by combing the band widths and the E_a values determined experimentally by the single crystals' ρ–T measurement. In the calculation for **3O**•$PF_6(CH_2Cl_2)_n$, we should estimate the 1D, half-filled, and dimerized band models divided into upper and lower Hubbard bands, assuming the symmetric density of state at around the Fermi energy, as illustrated in Figure S12a. From the depicted electronic structures, the U_{eff} of **3O**•$PF_6(CH_2Cl_2)_n$ can be calculated via the following equation:

$$U_{eff\_3O} = W_1 + W_2 + 2E_a + E_g \sim 1.30 \text{ eV} \qquad (1)$$

On the other hand, in the calculation for **2O**•PF_6, we should estimate 1D and half-filled band model, as illustrated in Figure 12b, and U_{eff} value can be calculated via the following equation:

$$U_{eff\_2O} = W + 2E_a \sim 1.53 \text{ eV} \qquad (2)$$

Compared to **2O**•PF_6, the U_{eff} values of **3O**•$PF_6(CH_2Cl_2)_n$ were lower by approximately 85%. We further discussed the insight of conjugation length-elongation effects. Despite the unfavorable dimerized band structure of **3O**•$PF_6(CH_2Cl_2)_n$, it showed superior conductivity to **2O**•PF_6, because of the smaller electronic correlation U_{eff} of **3O**•$PF_6(CH_2Cl_2)_n$ (U_{eff_3O} ~ 1.30 eV) compared to that of **2O**•PF_6 (U_{eff_2O} ~ 1.53 eV), leading to the following relationship.

$$U_{\mathrm{eff\_2O}} > U_{\mathrm{eff\_3O}} \quad (4)$$

According to an extended Hubbard model, U_{eff} is expressed as $U - 2V$ where U and V are on-site and inter-site Coulomb repulsions, respectively.

$$U_{\mathrm{eff\_2O}} = U_{\mathrm{2O}} - 2V_{\mathrm{2O}} \quad (5)$$

$$U_{\mathrm{eff\_3O}} = U_{\mathrm{3O}} - 2V_{\mathrm{3O}} \quad (6)$$

Combining the equations (4)–(6), the following inequality (7) can be deduced.

$$U_{\mathrm{2O}} - U_{\mathrm{3O}} > 2(V_{\mathrm{2O}} - V_{\mathrm{3O}}) \quad (7)$$

The increase of the averaged donor–donor distance for the single crystal of **3O**•$PF_6(CH_2Cl_2)_n$ than that for single crystal of **2O**•PF_6 (3.618 Å for **3O**•$PF_6(CH_2Cl_2)_n$ and 3.567 Å for **2O**•PF_6) suggests a smaller V for **3O**•$PF_6(CH_2Cl_2)_n$:

$$V_{\mathrm{2O}} > V_{\mathrm{3O}} \quad (8)$$

Thus, combining inequalities (7) and (8) deduced the following relationships between U_{3O} and U_{2O}.

$$U_{\mathrm{2O}} > U_{\mathrm{3O}} \quad (9)$$

, which was supported by the results of CV measurements. These data indicates that the improved conductivity for **3O**•$PF_6(CH_2Cl_2)_n$ compared to **2O**•PF_6 resulted from the decreased U based on the conjugation-length expansion, i.e., effects of the reduced U exceeded the unfavorable effects from the decreased V and W.

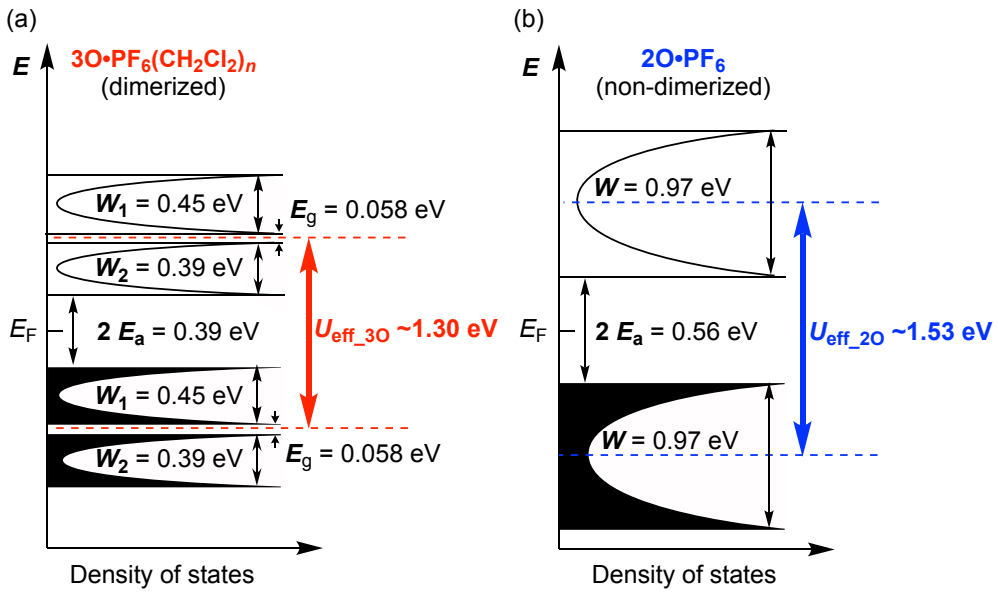

Figure S12. Estimated band structures with electronic correlation (a) **3O**•$PF_6(CH_2Cl_2)_n$ and (b) **2O**•PF_6.

12. Coordinates of optimized radical cations

Table S3. Geometry of optimized structure for **3O** (Figure S5a) from the DFT calculation.

C	3.9064263	4.5536591	-0.0381404
C	3.60064372	5.88839661	0.27585347
C	4.54475657	6.52081972	1.10304192
C	5.61541285	5.70209087	1.44490457
C	2.52525591	7.95035486	0.00308026
C	3.08155749	8.30897659	1.37269847
C	3.17011473	3.66173317	-0.8408139
C	3.49252418	2.32749401	-1.1532838
C	2.56311941	1.69278565	-1.9770112
C	1.46451138	2.49672946	-2.3347082
C	4.57153603	0.27906493	-0.8405531
C	4.04033082	-0.1005305	-2.2145363
C	7.9775524	4.73680431	2.55422018
C	0.37385133	2.1394006	-3.1501541
C	-0.7313555	2.92806243	-3.5102384
C	-1.66239	2.27917265	-4.3396091
C	-1.314856	0.96591271	-4.6367312
C	-2.7398588	4.31190163	-4.6863939
C	-2.2220888	4.72241573	-3.3162813
C	-1.3160656	-1.6196718	-5.6630114
H	3.13984462	8.38196611	-0.7953407
H	1.49271425	8.28701012	-0.105328
H	2.45448326	7.89083988	2.17006315
H	3.14903991	9.39185538	1.49317471
H	3.93864541	-0.1367558	-0.0475048
H	5.5986908	-0.065578	-0.7079287
H	4.68153014	0.30302749	-3.0072302
H	3.9650138	-1.1842815	-2.320399
H	8.8230626	5.0211903	3.18523708
H	7.44478432	3.90661098	3.02524669
H	8.35073629	4.44893991	1.56783866
H	-3.7622302	4.66382513	-4.8367521
H	-2.0962741	4.70846859	-5.4816488
H	-2.136655	5.80740111	-3.2343292
H	-2.873466	4.34236571	-2.5208326
H	-1.2196775	-2.0412523	-4.6589806
H	-1.8914952	-2.3098402	-6.2846937
H	-0.3329571	-1.4671446	-6.1159799
O	2.48847879	6.51262071	-0.1755339
O	4.42423251	7.80882709	1.52094434
O	4.6139795	1.71582825	-0.6925919
O	2.70110698	0.409393	-2.3984565
O	-2.7939597	2.87669099	-4.7988185
O	-0.8854913	4.20708771	-3.0974187
S	5.4462179	4.11174901	0.73288505
S	6.92675577	6.22849184	2.45587482
S	1.63650341	4.10287853	-1.6089598
S	0.20176238	0.52752981	-3.8797741
S	-2.2836465	-0.0697673	-5.6406752

Table S4. Geometry of optimized structure for **2O**$^{\cdot+}$ (Figure S5b) from the DFT calculation.

C	3.2761302	4.18263736	0.43078058
C	2.98640496	5.4708438	0.92406422
C	3.6213378	5.78187476	2.13334943
C	2.25862658	7.69058201	0.78304491
C	2.31574067	7.70101623	2.30291362
C	2.80238097	3.58580357	-0.747473
C	3.09210592	2.29759709	-1.2407565
C	2.45717637	1.9865677	-2.4500439
C	3.81988402	0.07785846	-1.0997376
C	3.76277362	0.06742585	-2.6196066
C	1.64308819	3.01647211	-2.9281419
C	4.43542718	4.75197088	2.61144675
C	-0.092462	4.51804052	-4.4995323
C	6.17097075	3.25039903	4.18284105
H	3.1524743	8.15419224	0.35098515
H	1.36578757	8.20023807	0.4175274
H	1.41044586	7.25611363	2.7330726
H	2.43702039	8.71778157	2.68040048
H	2.92603565	-0.385753	-0.6676805
H	4.71272259	-0.4317973	-0.7342184
H	4.66806961	0.51232851	-3.0497629
H	3.64149405	-0.949339	-2.997095
H	-0.6776298	4.48328334	-5.4215403
H	-0.7687131	4.66456311	-3.6533837
H	0.63221098	5.33342493	-4.5672558
H	6.75612193	3.28514833	5.10485992
H	5.44629368	2.43501654	4.25055203
H	6.84723207	3.10387744	3.33670118
O	2.16590776	6.33052415	0.28264602
O	3.46449439	6.96419887	2.7749
O	3.91260097	1.43791569	-0.5993371
O	2.61402119	0.80424404	-3.091595
S	4.40072604	3.36548931	1.53890957
S	1.6777855	4.40295182	-1.8556023
S	0.74537505	2.89677116	-4.4009226
S	5.33313981	4.87167129	4.08422771

13. NMR spectra

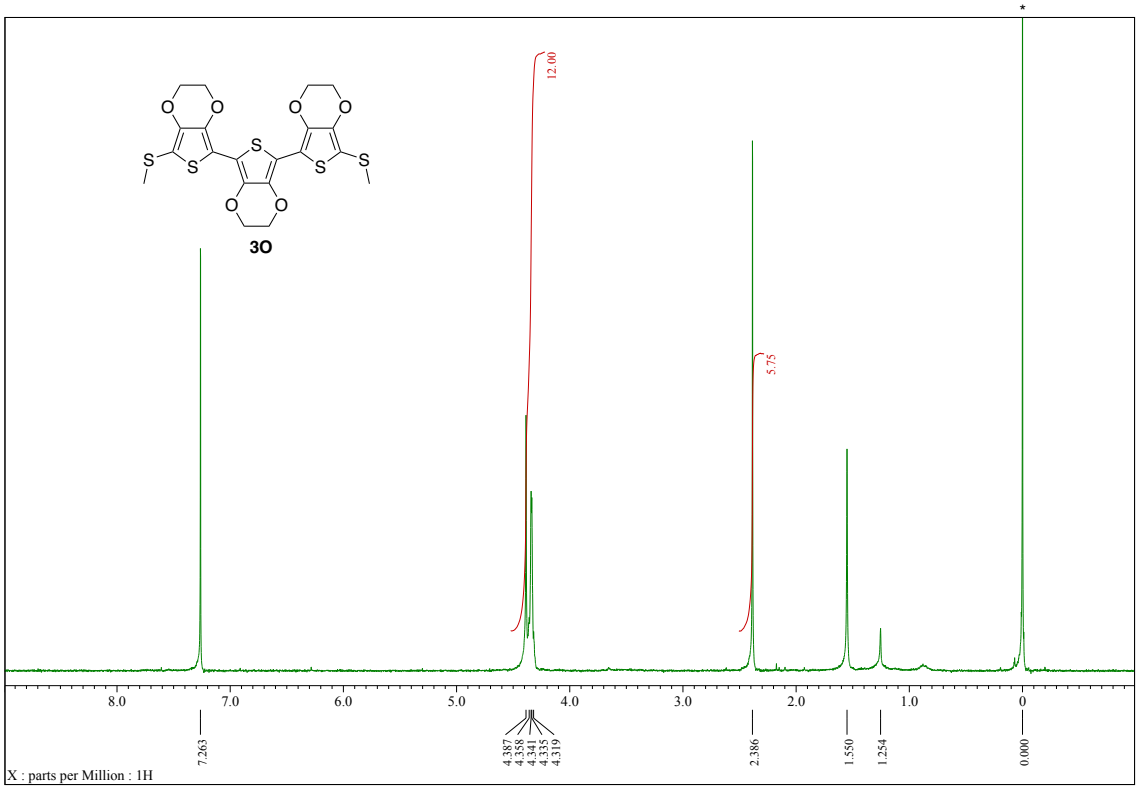

Figure S13. ^{1}H NMR spectrum of **3O** in $CDCl_3$. The signal for $Si(CH_3)_4$ used for the internal standard was shown with an asterisk.

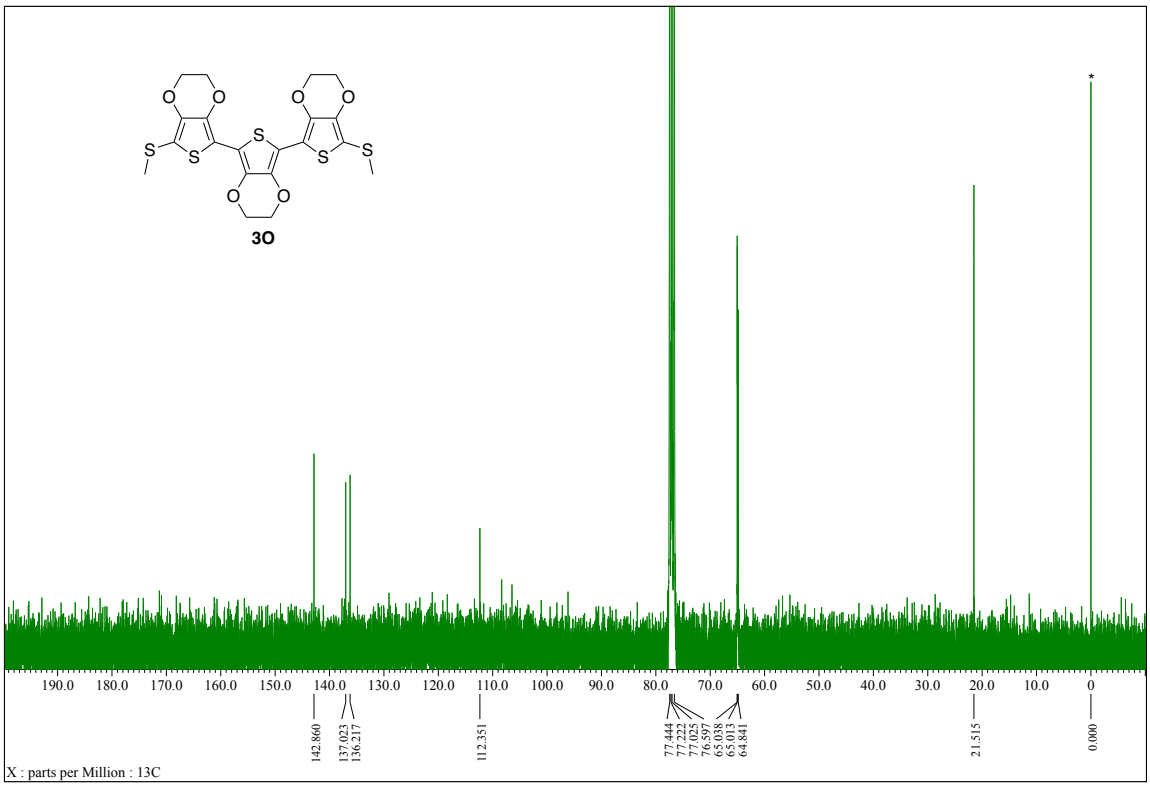

Figure S14. ^{13}C NMR spectrum of **3O** in $CDCl_3$. The signal for $Si(CH_3)_4$ used for the internal standard was shown with an asterisk.

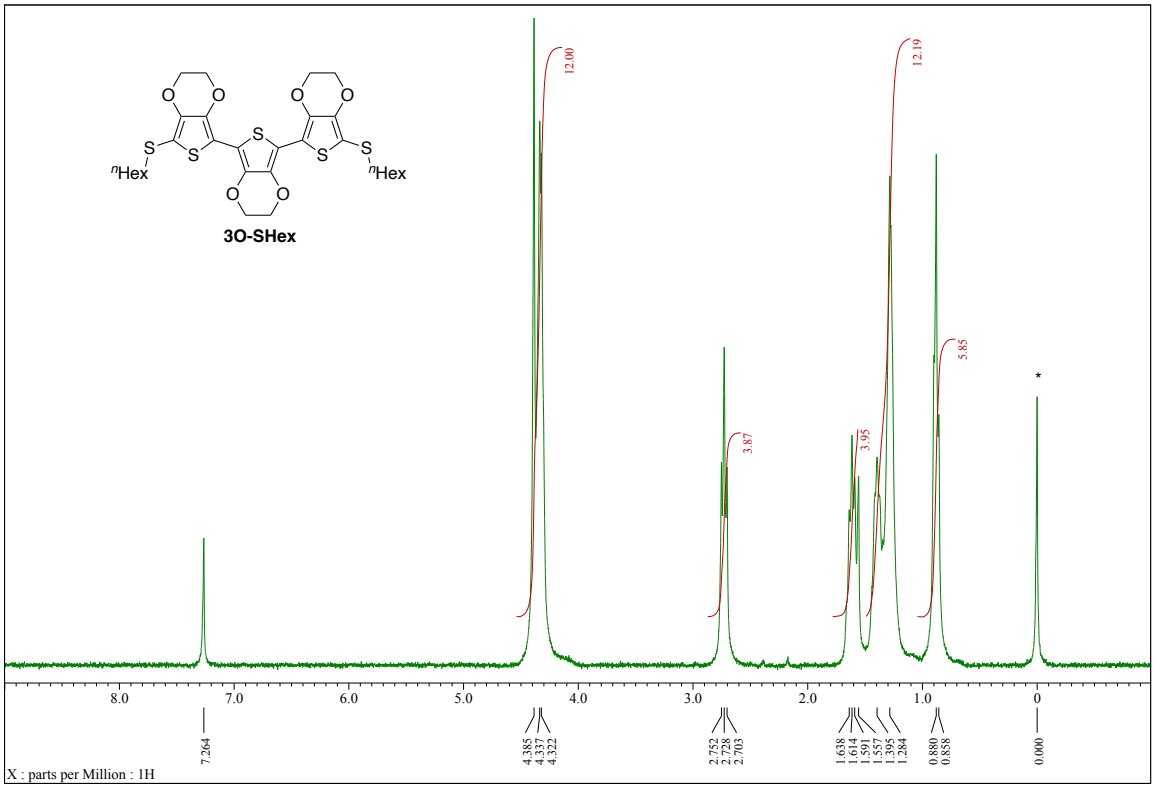

Figure S15. ^{1}H NMR spectrum of **3O-SHex** in $CDCl_3$. The signal for $Si(CH_3)_4$ used for the internal standard was shown with an asterisk.

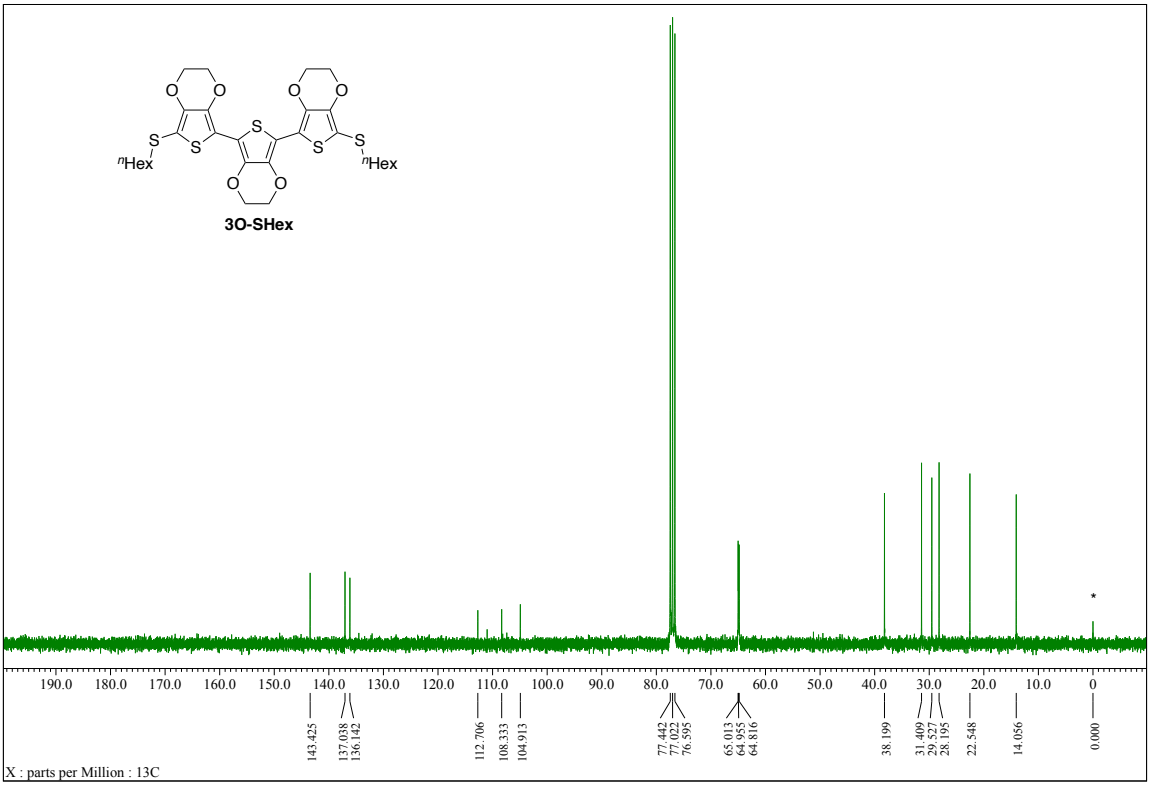

Figure S16. ^{13}C NMR spectrum of **3O-SHex** in $CDCl_3$. The signal for $Si(CH_3)_4$ used for the internal standard was shown with an asterisk.

1. W. C. Still, M. Kahn, A. Mitra, *J. Org. Chem*., **1978**, *43*, 2923–2925.
2. J. Hou, M.-H. Park, S. Zhang, Y. Yao, L.-M. Chen, J.-H. Li, and Y. Yang, *Macromolecules*, **2008**, *41*, 6012–6018.
3. D. T. Christiansen, A. L. Tomlinson, J. R. Reynolds, *J. Am. Chem. Soc.*, **2019**, *141*, 3859–3862.
4. T. Mathieu, H. Noemie, L. Philippe, F. Pierre, *Tetrahedron Lett.*, **2009**, *50*, 7148–7151.
5. C. D. Spicer, M. A. Booth, D. Mawad, A. Armgarth, C. B. Nielsen, M. M. Stevens, *Chem*, **2017**, *2*, 125–138.
6. M. Turbiez, D. Faye, P. Leriche, P. Frère, *New J. Chem.*, **2015**, *39*, 1678–1684.
7. G. M. Sheldrick, *Acta Cryst*., **2015**, *A71*, 3–8.
8. O. V. Dolomanov, L. J. Bourhis, R. J. Gildea, J. A. K. Howard, H. Puschmann, *J. Appl. Cryst*., **2009**, 42, 339–341.
9. Gaussian 09, Revision D.01, M. J. Frisch, G. W. Trucks, H. B. Schlegel, G. E. Scuseria, M. A. Robb, J. R. Cheeseman, G. Scalmani, V. Barone, G. A. Petersson, H. Nakatsuji, X. Li, M. Caricato, A. Marenich, J. Bloino, B. G. Janesko, R. Gomperts, B. Mennucci, H. P. Hratchian, J. V. Ortiz, A. F. Izmaylov, J. L. Sonnenberg, D. Williams-Young, F. Ding, F. Lipparini, F. Egidi, J. Goings, B. Peng, A. Petrone, T. Henderson, D. Ranasinghe, V. G. Zakrzewski, J. Gao, N. Rega, G. Zheng, W. Liang, M. Hada, M. Ehara, K. Toyota, R. Fukuda, J. Hasegawa, M. Ishida, T. Nakajima, Y. Honda, O. Kitao, H. Nakai, T. Vreven, K. Throssell, J. A. Montgomery, Jr., J. E. Peralta, F. Ogliaro, M. Bearpark, J. J. Heyd, E. Brothers, K. N. Kudin, V. N. Staroverov, T. Keith, R. Kobayashi, J. Normand, K. Raghavachari, A. Rendell, J. C. Burant, S. S. Iyengar, J. Tomasi, M. Cossi, J. M. Millam, M. Klene, C. Adamo, R. Cammi, J. W. Ochterski, R. L. Martin, K. Morokuma, O. Farkas, J. B. Foresman, D. J. Fox, Gaussian, Inc., Wallingford CT, **2016**.
10 (a) A. D. Becke, *Phys. Rev. A*, **1988**, *38*, 3098–3100; (b) A. D. Becke, *J. Chem. Phys*., **1993**, *98*, 5648–5652.
11. C. Lee, W. Yang, R. G. Parr, *Phys. Rev. B*, **1988**, *37*, 785–789.
12 (a) R. Ditchfield, W. J. Hehre, J. A. Pople, *J. Chem. Phys*., **1971**, *54*, 724–728; (b) W. J. Hehre, R. Ditchfield, J. A. Pople, *J. Chem. Phys*., **1972**, *56*, 2257–2261; (c) P. C. Hariharan, J. A. Pople, *Mol. Phys*., **1974**, *27*, 209–214.
13. T. Mori, A. Kobayashi, Y. Sasaki, H. Kobayashi, G. Saito, H. Inokuchi, *Bull. Chem. Soc. Jpn.*, **1984**, *57*, 627–633.
14. T. Ozaki, *Phys. Rev. B*, **2003**, *67*, 155108/1–155108/5.
15. T. Ozaki, H. Kino, *Phys. Rev. B*, **2004**, *69*, 195113/1–195113/19.
16. OpenMX: http://www.openmx-square.org/
17. K. Lejaeghere, G. Bihlmayer, T. Bjorkman, P. Blaha, S. Blugel, V. Blum, D. Caliste, I. E. Castelli, S. J. Clark, A. Dal Corso, S. de Gironcoli, T. Deutsch, J. K. Dewhurst, I. Di Marco, C. Draxl, M. Dulak, O. Eriksson, J. A. Flores-Livas, K. F. Garrity, L. Genovese, P. Giannozzi, M. Giantomassi, S. Goedecker, X. Gonze, O. Granas, E. K. U. Gross, A. Gulans, F. Gygi, D. R. Hamann, P. J. Hasnip, N. A. W. Holzwarth, D. Iu an, D. B. Jochym, F. Jollet, D. Jones, G. Kresse, K. Koepernik, E. Kucukbenli, Y. O. Kvashnin, I. L. M. Locht, S. Lubeck, M. Marsman, N. Marzari, U. Nitzsche, L. Nordstrom, T. Ozaki, L. Paulatto, C. J. Pickard, W. Poelmans, M. I. J. Probert, K. Refson, M. Richter, G.-M. Rignanese, S. Saha, M. Scheffler, M. Schlipf, K. Schwarz, S. Sharma, F. Tavazza, P. Thunstrom, A. Tkatchenko, M. Torrent, D. Vanderbilt, M. J. van Setten, V. Van Speybroeck, J. M. Wills, J. R. Yates, G.-X. Zhang and S. Cottenier, *Science*, **2016**, 351, aad3000.
18. T. Ozaki, H. Kino, *Phys. Rev. B*, **2005**, *72*, 045121/1–045121/8.
19. J. P. Perdew, K. Burke, and M. Ernzerhof, *Phys. Rev. Lett*., **1996**, *77*, 3865–3868.
20. K. Momma, F. Izumi, *J. Appl. Cryst*., **2011**, *44*, 1272–1276.
21. J. Yoshida, A. Ueda, A. Nakao, R. Kumai, H. Nakao, Y. Murakami, H. Mori, *Chem. Commun.* **2014**, *50*, 15557–15560.
22. G. A. Bain, J. F. Berry, *J. Chem. Educ.*, **2008**, *85*, 532–536.
23. R. Kameyama, T. Fujino, S. Dekura, M. Kawamura, T. Ozaki, H. Mori, *Chem. Eur. J.*, **2011**, *27*, 6696–6700.